



LAWRENCE
LIVERMORE
NATIONAL
LABORATORY

Modern Calculations of Pulsed-Sphere Time-of-Flight Experiments Using the Mercury Monte Carlo Transport Code

R. J. Procassini, M. S. McKinley

September 3, 2010

Joint International Conference on Supercomputing in Nuclear
Applications and Monte Carlo 2010 (SNA + MC2010)
Tokyo, Japan
October 17, 2010 through October 21, 2010

Disclaimer

This document was prepared as an account of work sponsored by an agency of the United States government. Neither the United States government nor Lawrence Livermore National Security, LLC, nor any of their employees makes any warranty, expressed or implied, or assumes any legal liability or responsibility for the accuracy, completeness, or usefulness of any information, apparatus, product, or process disclosed, or represents that its use would not infringe privately owned rights. Reference herein to any specific commercial product, process, or service by trade name, trademark, manufacturer, or otherwise does not necessarily constitute or imply its endorsement, recommendation, or favoring by the United States government or Lawrence Livermore National Security, LLC. The views and opinions of authors expressed herein do not necessarily state or reflect those of the United States government or Lawrence Livermore National Security, LLC, and shall not be used for advertising or product endorsement purposes.

Modern Calculations of Pulsed-Sphere Time-of-Flight Experiments Using the Mercury Monte Carlo Transport Code

Richard PROCASSINI and Michael Scott McKINLEY

Lawrence Livermore National Laboratory, P.O. Box 808, Livermore, CA 94551, United States of America

Modern Monte Carlo transport simulations of the Lawrence Livermore National Laboratory pulsed-sphere time of flight experiments have recently been performed^{1,2,3,4,5,6}. In these experiments, 14 MeV neutrons, generated via the $^3\text{H}(d, n)^4\text{He}$ reaction, interact with a sphere of material that surrounds the neutron generating target. The time of arrival of the uncollided and collided neutrons are recorded in a detector system placed up to 10 meters from the center of the sphere. A collection of experiments with varying sphere materials, mean-free-paths and detector systems have been modeled using the *Mercury* Monte Carlo transport code^{7,8}. This effort serves to validate new features of the *Mercury* code, including general sources, tallies and point-detector / biased-collision variance reduction methods, as well as assess the quality of evaluated nuclear data sets^{9,10,11,12,13}. In general, the level of agreement between the calculations and experiment is very good. However, for certain pulsed spheres, discrepancies are observed between the simulations using different nuclear data sets.

KEYWORDS: *Monte Carlo, particle transport, pulsed spheres, time of flight experiments, tallies, variance reduction.*

I. Introduction and Motivation

The pulsed-sphere time of flight experiments performed at the Lawrence Livermore National Laboratory (LLNL) from the late 1960s through the early 1990s were designed to measure the leakage spectra of 14 MeV neutrons from spherical targets of various materials¹⁻⁶. Data obtained from these experiments has been used in the past to validate the physics in neutron transport codes, as well as guide the evaluation of nuclear data libraries^{14,15,10,16}. This paper details a recent effort to model several pulsed sphere experiments using the *Mercury* Monte Carlo particle transport code^{7,8}. *Mercury*, which is currently being developed at LLNL in support of a variety of laboratory missions, was used to model a large collection of pulsed sphere experiments comprised of various sphere materials, of varying optical depths, with multiple detector systems.

There are three motivations for performing this study. First, the pulsed spheres constitute an ideal set of experiments with which to validate several new features in *Mercury*. These features include (a) ion charged-particle transport, (b) user-defined sources and tallies, and (c) point-detector (biased collision) variance reduction methods. Next, this study demonstrates *Mercury*'s capability to model other time-of-flight experiments. For example, the National Ignition Facility (NIF) inertial confinement fusion (ICF) facility is currently developing two neutron time-of-flight (NTOF) diagnostic beam lines which will be modeled with *Mercury*¹⁷. Lastly, these experiments permit an assessment of quality of several evaluated nuclear data libraries that are available to users at LLNL. The goals of the study were to (a) examine cross section differences amongst various evaluations over a wide range of neutron energies, (b)

uncover potential errors in data translation and library processing, and (c) motivate future evaluation efforts based upon observed computation to experiment ratios.

This paper is organized as follows. The pulsed-sphere experimental configuration and *Mercury* computational methodology are described in Section II. In Section III, the techniques used to characterize the energy and angle spectra of the 14 MeV neutron source in these experiments are discussed. The results of the *Mercury* time-of-flight calculations are presented in Section IV. Finally, Section V summarizes the current effort and suggests futures areas of investigation.

II. Experimental Configuration and Computational Methodology

The pulsed sphere experiments were initiated when a pulsed beam of deuterons ($^2\text{H}^+$) was accelerated to 400 keV in the Insulated Core Transformer (ICT)¹. The high energy deuterons were directed onto a tritiated-titanium disk at the end of the target assembly, generating 14 MeV neutrons via the $^3\text{H}(d, n)^4\text{He}$ reaction. These neutrons interacted with a sphere of material that was placed around the target assembly. The time of arrival of the uncollided and collided neutrons exiting the sphere was then recorded by a detector system placed up to 10 meters from the center of the sphere.

A schematic drawing of the complete experimental configuration, including the accelerator, beam transport system, target and pulsed sphere assemblies, collimators and detector assembly, is shown in **Figure 1**. The experimental pit was a 10.24 meter cubic room surrounded by 2.02 meter thick concrete walls. A detailed schematic of the experimental pit is shown in **Figure 2**. The pulsed sphere and target assemblies were located close to the center of the

¹ Corresponding Author E-Mail: spike@llnl.gov

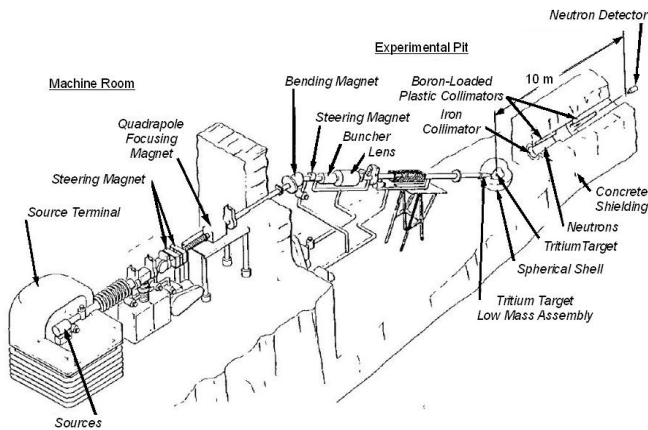


Fig. 1 Schematic view of the ICT accelerator, beam transport system, target and pulsed sphere assemblies, collimators and detector assembly (not to scale).

pit. The amount of mass in the vicinity of the pulsed sphere and detector was minimized in order to reduce the effects of background scattering. Two of the walls had a cylindrical tunnel connecting the experimental pit to the detector room. These tunnels were oriented at 26, 30 and 120 degrees to the path of the deuteron beam (see Figure 2)¹. A conical collimator assembly was inserted into each tunnel to further minimize the scattered neutron signal reaching the detector. Finally, the arrival time of the neutrons was recorded by the detector assembly.

In the *Mercury* simulations of the pulsed sphere experiments, only the experimental pit is modeled, however, without the relevant components of the beam transport system. A cutaway view of the computational geometry model of the pulsed-sphere experimental pit used in the *Mercury* simulations is shown in **Figure 3**. This complex system was modeled using the 3-D combinatorial geometry capability in *Mercury*. This model includes the front and rear walls, the target and pulsed sphere assemblies, the conical collimator assembly embedded in the front wall, a

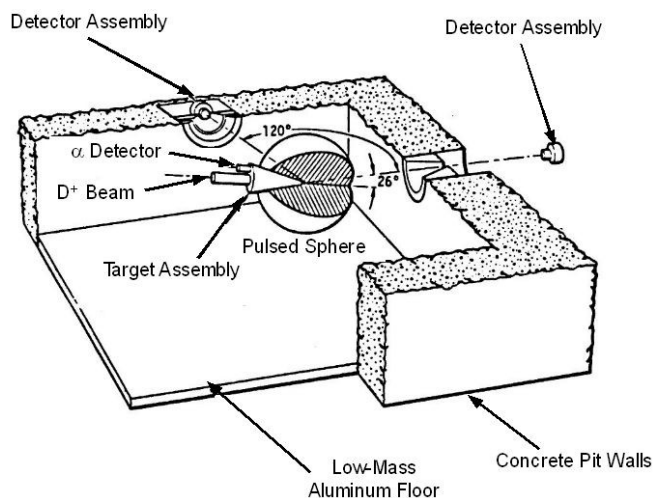


Fig. 2 Detailed schematic view of the target assembly, pulsed sphere and experimental pit (not to scale).

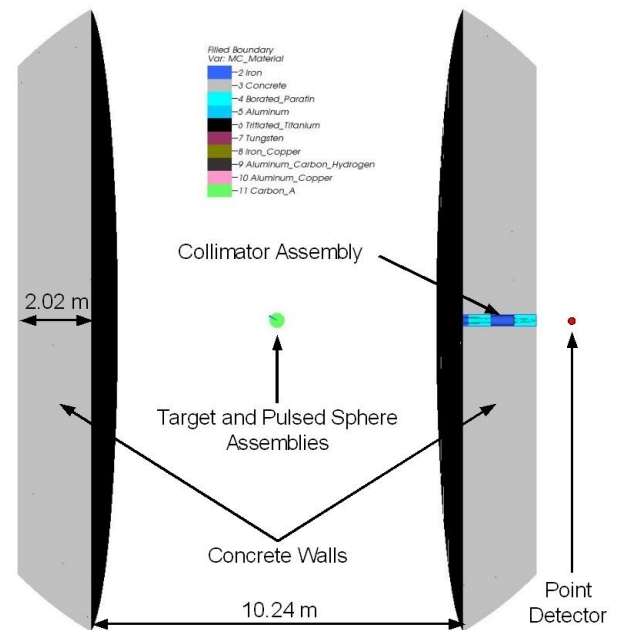


Fig. 3 The *Mercury* computational geometry model of the pulsed-sphere experimental pit, including the target and pulsed sphere assemblies, concrete walls, collimator assembly and point detector.

point detector, plus the surrounding air, all within an $r = 10$ meter spherical “universe”. The system is centered on the tritiated-titanium disk at the end of the target assembly. A leakage boundary condition is enforced at the edge of the spherical universe.

Detailed views of the front wall and collimator assembly, and the target and pulsed sphere assemblies are shown in **Figures 4** and **5**, respectively. The collimator assembly (Figure 4) consists of an iron pipe that is inserted into the tunnel in the front wall, along with one iron and two borated-paraffin conical sections. These act to absorb and moderate neutrons, as well as to focus them onto the detector. The detector system is modeled as a *point detector* surrounded by an $r = 0.25$ cm acceptance sphere. A description of the point detector methodology is included later in this section. The low-mass target assembly (Figure 5) consists of a thin conical and cylindrical section of aluminum. The aluminum-copper mounting disk at the rear (left) of the assembly provides mechanical stability, while the thin target disks are mounted at the front (right) of the assembly. An aluminum drift tube prevents the deuterons from hitting the conical wall of the target assembly and directs them towards the target disk. The pulsed sphere includes a conical hole, such that it may be slid onto the target assembly. Various pulsed sphere designs were developed during the course of the experimental program¹⁻⁶. The carbon pulsed sphere shown in Figure 5 is one of the simplest one component designs.

Neutrons are sourced into the system at a point in the center of the tritiated-titanium disk. The temporal response of the source is assumed to be Gaussian with a FWHM in the range $0.3 \leq \tau_{FWHM} \leq 3.7$ nsec. The assumed Gaussian

behavior is due to the lack of experimental documentation. The energy and angle spectra of the source neutrons are described in the following section.

The *Mercury* time-of-flight calculations of the pulse sphere system employed both *transport* and *diagnostic* particles. Transport particles are the “classic” Monte Carlo particles. These neutrons undergo collisions, in the process creating both transport and diagnostic neutrons. In contrast, diagnostic particles are *rays* that (a) are directed towards the center point of the detector with a reduced weight, in accordance with the probability of emission in the direction of the detector, and (b) undergo weight attenuation along the path between creation and tally events to simulate both collision attenuation and $1/r^2$ spreading.

The different tracking methods employed for transport and diagnostic particles are shown schematically in **Figure 6**. Transport particle tracks are shown in blue, while diagnostic particle tracks are shown in red. The weight of the particle is represented by the thickness of the line segment. A single transport neutron (Transport) of weight w and energy E is emitted from the point source and travels some distance through the pulsed sphere before it experiences a collision (Collision 1). The transport particle exits the collision traveling in a slightly different direction relative to the incident particle. In addition, a diagnostic particle (Diagnostic 1) is emitted at the collision site, however, this particle is directed towards the point detector. Since the direction of the point detector differs from that of the outgoing transport particle by the angle θ_1 , the weight of the Diagnostic 1 is modified to account for the relative probabilities of emission in the two directions (red vs blue). Therefore, Diagnostic 1 is created with a weight $w_1 < w$. All diagnostic particles undergo weight attenuation as they travel to the point detector.

Since diagnostic particles do not experience any

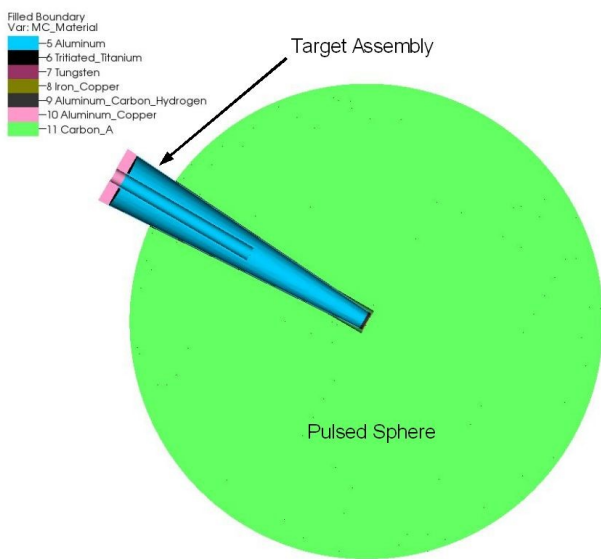


Fig. 5 A detailed view of the target and pulsed sphere assemblies in the *Mercury* computational geometry model of the pulsed-sphere experimental pit.

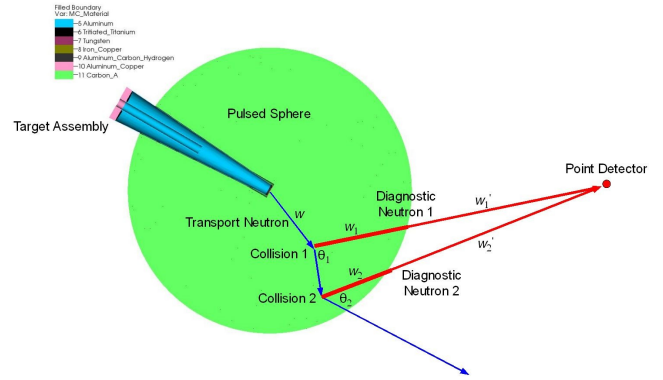


Fig. 6 The different nature of particle tracking for transport and diagnostic particles is shown schematically. Transport particle tracks are shown in blue, while diagnostic particle tracks are shown in red. The weight of the particle is represented by the thickness of the line segment.

collisions, the energy of the diagnostic particle remains constant at that of the transport particle exiting the collision (E_1). As Diagnostic 1 exits from the sphere, the weight of the particle is reduced to $w'_1 < w_1$ to account for collision attenuation and $1/r^2$ spreading. Similarly, as Diagnostic 1 enters the point detector sphere after traveling through air, its weight is reduced to $w''_1 < w'_1$. This amount of weight is then scored in the detector tally at a time corresponding to the time of emission plus the time of first collision plus the time of flight to the detector at the energy E_1 :

$$t_{\text{tally}} = t_{\text{emit}} + t_{\text{coll } 1} + \Delta x / v(E_1) \quad (1)$$

where t_{tally} is the tally time, t_{emit} is the emission time from the source, $t_{\text{coll } 1}$ is the time of Collision 1, Δx is the distance from the site of Collision 1 to the point detector and $v(E_1)$ is the speed of a neutron with energy E_1 . When the transport particle experiences a second collision (Collision 2) within the sphere, another diagnostic particle (Diagnostic 2) is created, launched towards the point detector and the process repeats itself. Each diagnostic particle that is created at a transport-particle collision site will track all the way to the point detector and contribute to the tally, albeit with a weight that is significantly reduced from its birth weight. Note that the number of collisions that a transport particle experiences between creation of a diagnostic particle may be set by the user to improve the efficiency of the calculation.

The use of diagnostic particles with angle-biased collisions and a point detector constitutes, in effect, a variance reduction method. For a reasonable number of particle histories, this method produces point detector tallies with significantly reduced statistical noise relative to analog transport simulations. The point detector tally used in the pulsed-sphere time-of-flight simulations is set to respond only to diagnostic particles. This ensures that any transport particles that are “lucky enough” to travel through the collimator assembly and enter the point detector sphere will not be tallied. In addition, cutoff variance reduction methods are employed to prevent the generation of

diagnostic particles in the vicinity of the point detector. If this measure is not taken, the time of flight spectra exhibit anomalous, random spikes. These arise when transport particles collide within the collimator assembly or air surrounding the detector, producing diagnostic particles whose weight at the point detector is not sufficiently diminished by $1/r^2$ spreading.

Previous modeling efforts have utilized a *spherical* wall and a conical ring detector to improve the signal to noise ratio, relative to the actual geometric configuration, in transport-particle based calculations^{14,18}. In contrast, our model (currently) only includes the front and rear walls, omitting the side walls, ceiling and floor. Since the point detector in our model only responds to diagnostic particles and the collimator is included, it is highly unlikely that scatters in those components would provide any contribution to the tally signal. However, it is possible for a particle to scatter off of the rear wall, generating a diagnostic particle that would travel through the collimator opening and contribute to the point detector tally. In the future, our model will be extended to include the missing components, so we may assess their impact on the observed experimental signal.

III. Characterization of the Neutron Source

Since the outset of the pulsed-sphere experimental program, the energy and angle dependence of the 14 MeV neutron source have been described with varying degrees of complexity and physical realism^{1,14}. The earliest models assumes that the emission energy was monoenergetic at each emission angle, where any energy spread was incorporated into the time response of the source¹. Later models were much more sophisticated. In particular, Marchetti and Hedstrom used a multi-step process, which modeled the deuteron implantation into the target with the **TRIM** code to determine the average energies of the ions, used tabulated $^3\text{H}(\text{d}, \text{n})^4\text{He}$ cross sections and non-relativistic kinematics to produce a correlated energy-angle spectrum^{14,19}. This spectrum exhibited a narrow-energy-width, high-intensity peak for $E_n \sim 14.1$ MeV and emission at 0 degrees relative to the incident beam. This corresponds to the most probable energy of neutrons produced in the $^3\text{H}(\text{d}, \text{n})^4\text{He}$ reaction ($Q = 17.59 \text{ MeV}$) For forward or backward emission, the spectrum becomes broader in energy, with non-zero contributions at 0 and 180 degrees.

Instead of using the source spectrum of Marchetti and Hedstrom, our approach was to obtain the spectrum from a single **Mercury** charged-particle transport calculation. The interaction of a 400 keV deuteron beam from the ICT accelerator was modeled as it impinges upon a 10 μm thick tritiated-titanium target. Deuteron energy loss via both small-angle Coulomb and large-angle nuclear scattering was modeled. Since, at the time, **Mercury** did not include an ion deflection capability, the deuterons slowed down in a straight line trajectory that was normal to the surface of the target. In addition, transmutation, or reaction-in-flight,

nuclear collisions were also modeled, these being the source of the 14 MeV $^3\text{H}(\text{d}, \text{n})^4\text{He}$ neutrons. The calculation also modeled knock-on effects: the up scattering of deuterons and tritons (produced by the $^3\text{H}(\text{d}, \text{n})^4\text{He}$ reaction) that were previously deposited into the background. While inclusion of this effects increases the amount of reactions-in-flight, its contribution is negligible to the overall neutron production.

In an attempt to determine the range of the 400 keV deuteriums within the 10 μm thick tritiated-titanium disk, it was subdivided into layers $\Delta = 0.1 \mu\text{m}$ thick. A forced-collision variance reduction algorithm was employed to ensure that some neutrons were produced within each layer. The source characterization calculation was run with 10^9 deuteron particle histories. This resulted in the production of 1.1917×10^8 neutrons, which is more than sufficient to determine the correlated energy-angle dependence of the neutron source. The range of the deuterons in the disk was in the range $1.7 \leq L \leq 1.8 \mu\text{m}$, hence, none of the deuterons exited out the back of the target. Upon creation, neutrons were tallied into a correlated set of 36 bins with energies in the range $12.6 \leq E_n \leq 16.0$ MeV, and 20 bins with angles in the range $-1 \leq \mu \leq 1$, where $\mu = \cos \theta$ for scattering angle θ . This data defined the energy-angle dependence of the neutron source in the suite of time of flight calculations.

The energy and angle spectra of the neutron source are shown in **Figures 7 and 8**, respectively. Figure 7 indicates the neutron source has a broad maximum of nearly constant magnitude within $\Delta E \sim 0.5$ MeV of the most probable neutron energy for the reaction ($\bar{E} = 14.07 \text{ MeV}$). Outside of this energy range, the spectrum falls off in a nearly symmetric manner. The spectrum reaches zero 1.3 MeV (1.5 MeV) from the most probable energy on the low-energy (high-energy) side of the spectrum.

The calculated angle spectrum are shown by the **blue** triangles in Figure 8. Although there is some scatter in these results, the spectrum can be characterized as linearly varying. This is borne out by the **red** curve, which is a linear fit for the **blue** triangles. This conclusion is not in agreement with Figure 5 of Wong, et al., where that curve exhibits an asymptotic behavior within ~ 60 degrees of $\mu = \pm 1$. The black '*' and '+' data points in Figure 8 are data obtained from an experiment in which a beam of D^+ ions are injected into a T_2 gas target²⁰. The slope of the **red** line is much shallower than the locus of '+' data points, indicating that the average energy of deuterons inducing $^3\text{H}(\text{d}, \text{n})^4\text{He}$ reaction is much lower than 500 keV. The **red** line is slightly shallower than the locus of '*' data points, hence, it can be stated that the average energy of the deuteron creating neutrons in the simulation is less than 200 keV. This energy is less than the injected beam energy due to the energy loss associated with small- and large-angle Coulomb collisions and nuclear elastic collisions. While our conclusions (linear behavior, $\langle E_d^{\text{react}} \rangle < 200$ keV) are generally in agreement with those of Marchetti and Hedstrom, our linear fit is closer to the 200 keV '*' data points, while their fit is much shallower than the **red** line in Figure 8. They concluded the average deuteron energy inducing reaction was 100 keV¹⁴.

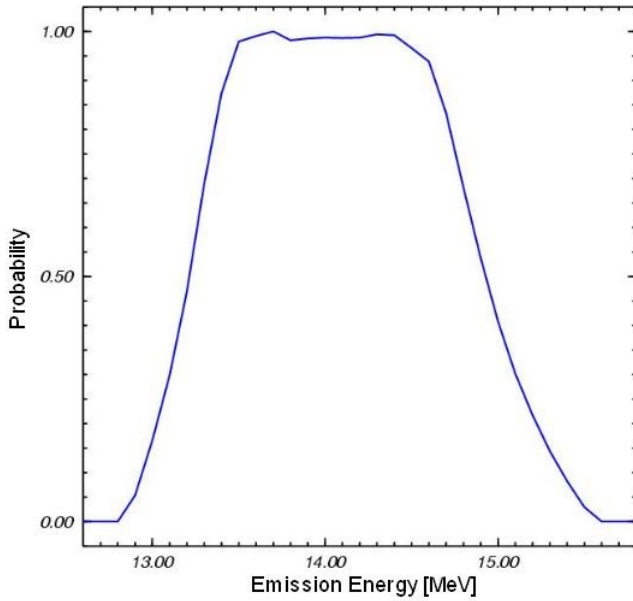


Fig. 7 The energy spectrum of neutrons emitted by the $^3\text{H}(d, n)^4\text{He}$ reaction in the *Mercury* calculation of deuterons impinging upon the tritiated-titanium target.

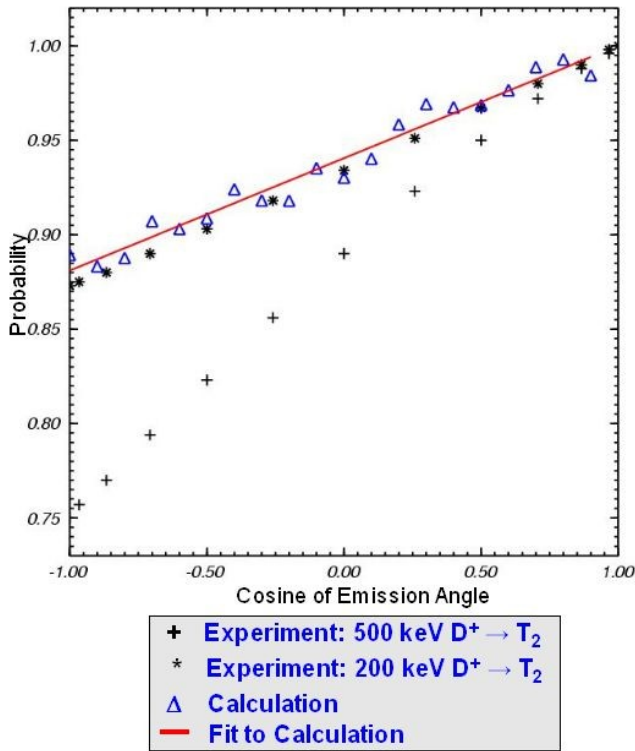


Fig. 8 The angular spectrum of neutrons emitted by the $^3\text{H}(d, n)^4\text{He}$ reaction in the *Mercury* calculation of deuterons impinging upon the tritiated-titanium target. The black '*' and '+' data points are experimental results obtained from the injection of D^+ ions into a D-T plasma. The blue triangles are the result of the *Mercury* calculation, and the red line is a linear fit to the calculated results.

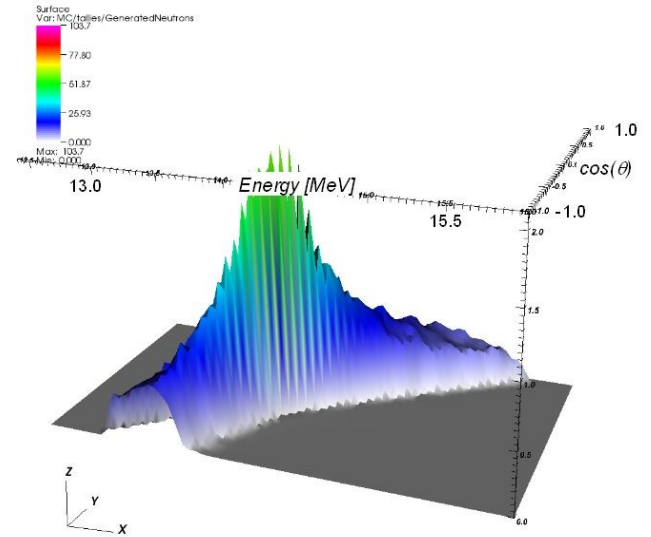


Fig. 9 The correlated energy-angle spectrum of neutrons emitted by the $^3\text{H}(d, n)^4\text{He}$ reaction in the *Mercury* calculation of deuterons impinging upon the tritiated-titanium target.

Our best estimate of this quantity was obtained by tallying the energy of each deuteron that produces a neutron. The resultant tally increases nearly linearly with deuteron energy. When these results were fit to a line, the median energy of deuterons that produce neutrons was found to be $\langle E_d^{\text{react}} \rangle = 197.9 \text{ keV}$.

The three-dimensional surface plot of the correlated energy-angle source spectrum is shown in Figure 9. The jagged nature of the this surface plot near the peak of the spectrum is an plotting artifact that is a consequence of the “narrowness” of the spectrum. Near the peak, the spectrum forms a narrow ridge that contributes to only one or two tally bins, and the ridge runs across the bins at ~ 45 degrees to either axis. To confirm that this result is indeed an artifact, the number of tally bins in each direction was doubled, resulting in a reduction of, but not elimination of the, the

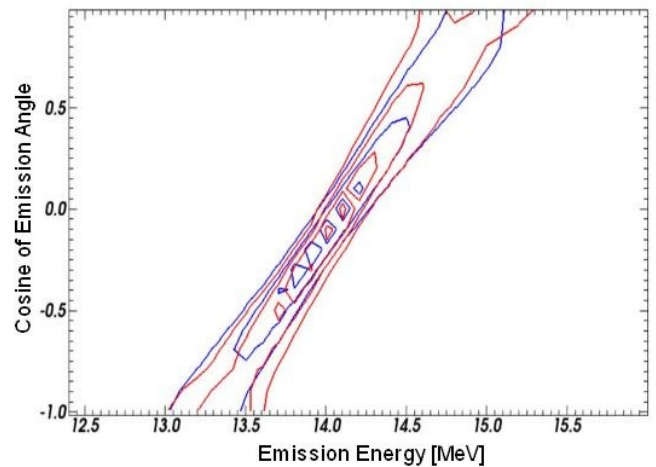


Fig. 10 Comparison of the correlated energy-angle spectra of neutrons emitted by the $^3\text{H}(d, n)^4\text{He}$ reaction. The spectrum from *Mercury* is shown in blue and the spectrum of Marchetti and Hedstrom is shown in red.

artifact. The general shape of the surface shown in Figure 9 is qualitatively similar to that presented in Figure 4 of Marchetti and Hedstrom, who utilized the same tally bin limits and bin resolution. For a more direct comparison, consider Figure 10, which shows contour plots of both data sets overlaid on each other: the current results are shown in blue, while those of Marchetti and Hedstrom are shown in red. There is rather good agreement between the two sets of results. The noticeable differences are a slight tilt in their data relative to ours, and their energy distributions in the vicinity of $\mu \pm 1$ are somewhat wider than ours. Overall, the complex, multi-step process used by Marchetti and Hedstrom resulted in a rather accurate description of the energy and angle dependence of the neutron source. Having calculated the source neutron spectrum, it was used to inject particles into the neutron time-of-flight calculations.

IV. Results of the Pulsed-Sphere Time-of-Flight Calculations

A collection of 56 pulsed sphere experiments, composed of varying sphere materials, optical depths and detector systems, were simulated with *Mercury*. A wide variety of sphere materials were modeled, including molecular liquids at room temperature (H_2O), cryogenic molecular liquids (O_2 , N_2), molecular solids (polyethylene CH_2 , Teflon CF_2), isotopically enriched materials (6Li , 7Li , $^6Li^2H$, ^{235}U , ^{238}U , ^{239}Pu) and elemental materials (Be, C, Al, Fe, Cu, Nb, Sn, Ho, Ta, W, Au, Pb, Th). The spheres were of varying radii, with optical depths in the range $0.5 \leq r/\lambda \leq 4.9$ mean-free-path (mfp) lengths.

Typical pulsed sphere designs are shown in Figures 11 and 12. These figures illustrate pulsed sphere configurations that are simple and complex, respectively. Two background characterization experiments were also simulated, in which no sphere was placed onto the target assembly. The experiments that were simulated used one of two distinct types of neutron detection systems: an NE213 liquid scintillator or a stilbene crystal plastic scintillator. Depending upon the scintillator chosen, the detectors were electrically biased to record neutrons with energies above a threshold value, which was set in the range $0.8 \leq E_{bias} \leq 3.0$ MeV. In addition to the detector biases, the energy-dependent detector efficiencies were also included in the simulations. The detector efficiencies for the two detector systems and various bias settings are shown in Figure 13. The NE213 detector efficiencies are shown in blue, while those for the stilbene detector are shown in red. The dotted curves have a 0.8 MeV bias, the dashed curve has a 1.6 MeV bias and the solid curves have a 3.0 MeV bias. Each pulsed sphere configuration that was simulated with *Mercury* used 10^7 particle histories for each of five different nuclear data sets: ENDL-94⁹, ENDL-2008.2¹⁰, ENDF/B-VII¹¹, JEFF-3.1¹² and JENDL-3.3¹³.

1. Background Characterization

The experimental and simulated time-of-flight spectra for a background characterization experiment are shown in

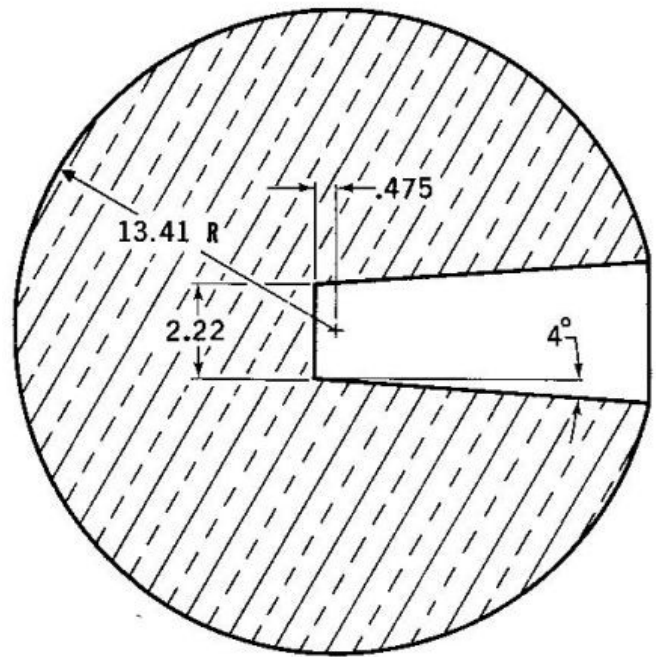


Fig. 11 A cutaway view of a simple pulsed sphere configuration. This design was typically used for metallic materials.

Figure 14. Before discussing the results, let us examine some features of the figure that shall be repeated for all of the time-of-flight spectra that will follow. The data/results are plotted as a function of the neutron arrival time at the detector, where zero time is when the deuterons begin to impinge upon the tritiated-titanium target. The spectrum is given in units of normalized count rate (neutrons recorded at the detector per nsec per source neutron). The time-of-flight spectra typically have a large, narrow peak at early times (centered on 14 MeV) that is produced by the uncollided

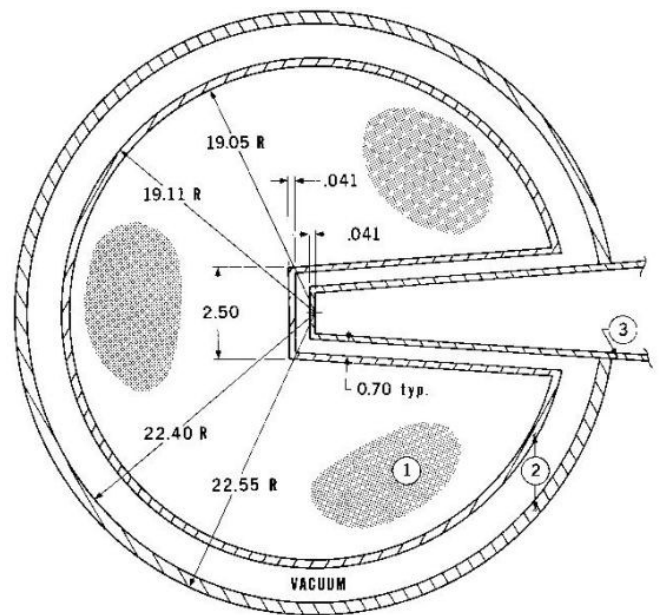


Fig. 12 A cutaway view of a complex pulsed sphere configuration. This design was used for cryogenic molecular liquids.

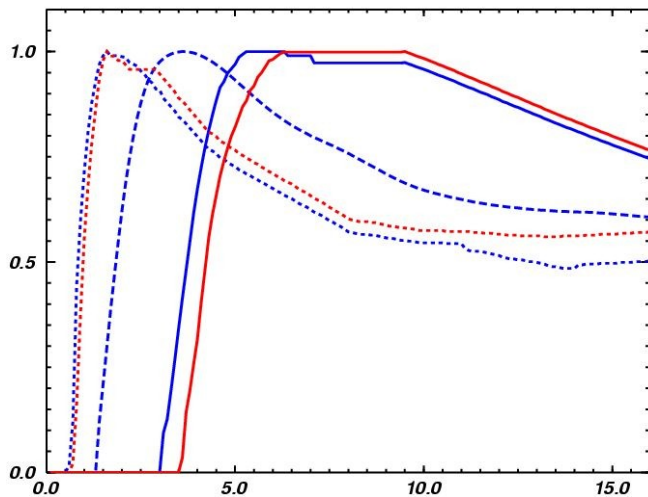


Fig. 13 Detector efficiency curves for the two detector systems and various bias settings. NE213 detectors are shown in blue, while stilbene detectors are shown in red. The detector biases are 0.8 MeV (dotted curves), 1.6 MeV (dashed curve) and 3.0 MeV (solid curves).

neutrons, followed at later times (lower energies) by a broad distribution that is produced by collided neutrons.

The experimental data points are shown as blue circles. The simulated results are shown as solid curves, where the color denotes the nuclear data set used in the calculation: ENDL-94 is red, ENDL-2008.2 is gray, ENDF/B-VIII is violet, JEFF-3.1 is gold and JENDL-3.3 is turquoise. Additional details about the experiment are provided below the legend box, including the flight path distance from the target to the point detector, the angle of the collimator line-of-sight relative to the incident deuteron beam, and the detector system with the applied bias. Finally, a series of energy fiducials are plotted at the bottom of the figure. Each set of simulated results has been normalized to the time integral of the experimental spectrum over the entire domain

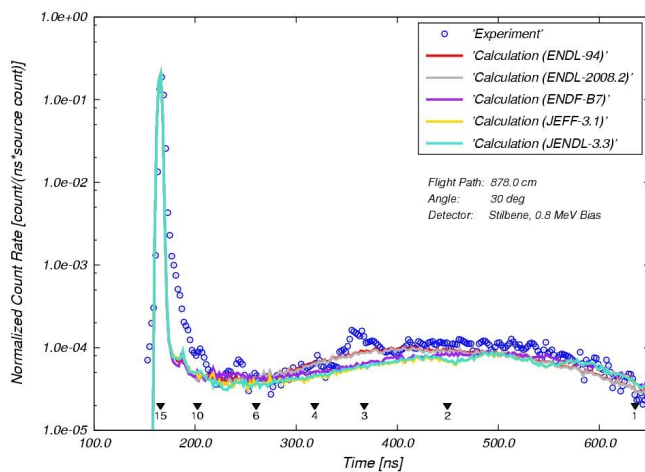


Fig. 14 The experimental and simulated time-of-flight spectra for a background characterization experiment. The experimental data is shown by the blue circles, while the solid curves are obtained from *Mercury* calculations using different nuclear data sets.

of experimental times. Only two experiments required a different normalization method. In these cases, the standard normalization method produced maximum values of the uncollided neutron peak in the data and results that differed significantly. In order to weight the time integration to high energies (early times), the modified normalization method only integrated over energies $E_n \geq 10$ MeV.

The various simulation results are in good agreement with the data near the maximum of the uncollided peak. However, the simulations produce a narrower peak than is seen in the experiment, with significant differences on the back (low energy) side of the peak. While no explanation for this discrepancy can be provided, this behavior has also been observed in simulations of background (no-sphere) experiments using the *Tart* Monte Carlo code (see Figures 10 and 11 of Reference 14)²¹. There is some variability in the results for lower energies $E_n \leq 5$ MeV, where on average, the ENDL data sets provide better agreement with the data than the other data sets. This level of agreement is sufficient to consider the simulation methodology validated for (no-sphere) background experiments.

Note the small peak in the data in the vicinity of $E_n \sim 3$ MeV. This feature arises from neutrons generated by the $^2\text{H}(d, n)^3\text{He}$ reaction within the target disk⁶. The presence of deuterium within the target is a result of injected deuterons that were thermalized and deposited there during prior experiments. This feature is not included in the simulated time-of-flight spectra because it was not possible to determine the deuterium concentration in the target from any publications or laboratory reports. As a result, no deuterium was loaded into the target disk in the simulations.

A selection of pulsed sphere results is presented below, spanning the wide variety of target materials simulated. Results for at least one experiment in each class of materials is shown. Those systems which exhibited anomalous results are discussed, while those system which have reasonable simulation to experiment agreement are presented for the reader's perusal.

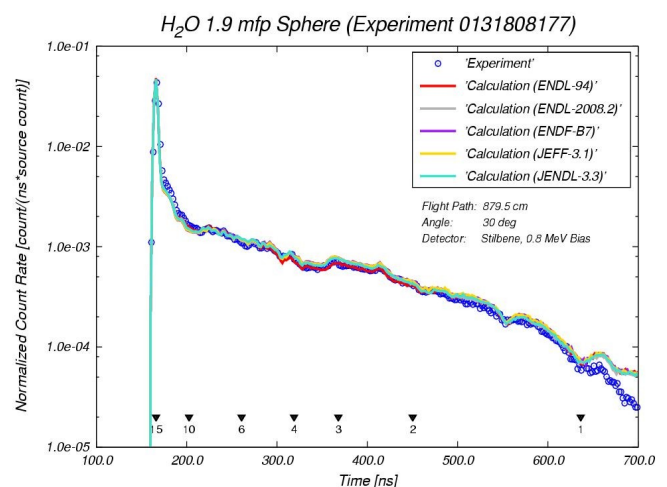


Fig. 15 The experimental and simulated time-of-flight spectra for a 1.9 mfp water (H_2O) sphere.

2. Molecular Liquids: Water

The simulated results and experimental data for a 1.9 mfp water (H_2O) sphere are shown in **Figure 15**. The agreement between the simulated results and experimental data is excellent for $E_n > 1$ MeV. In fact, this experiment exhibits the highest level of agreement of any pulsed sphere modeled. The simulations are slightly narrower on the back side of the peak, and other discrepancies are within a few standard deviations of the experimental statistic spread.

Despite the high level of agreement for $E_n > 1$ MeV, the simulation results are significantly above the experimental data below that energy. Differences between the data and results at low energies have been noticed in simulations of several pulsed sphere experiments, as seen below. At first, it was thought that this difference might be due to collisions of low-energy transport particle within the collimator assembly, but outside of the region in which the cutoff variance reduction method was being applied. However, the observed behavior is smoother than the random spikes that this cutoff method was intended to resolve. Late in the process of writing this paper, it was discovered that there are three potential causes for this behavior.

First, the file containing the experimental data that was used to (a) create these plots and (b) define the simulation model of the experiment contains an inconsistency in the definition of the angle between the deuteron beam and the collimator axis. In particular, the angle for this experiment is stated to be 26 degrees and 30 degrees in the meta data header. Unfortunately, the 30 degrees was chosen, when apparently, the true geometry had a 26 degree offset²². Second, when the model of the geometry was developed, the *entire* environment outside of the target and pulsed sphere assemblies (collimator assembly, point detector and walls) was rotated by this angle. An accurate specification of this geometry would have been to rotate the collimator assembly and point detector, but to leave the walls fixed. Third, the experimental data file provided data points for this experiment out to $t = 755$ nsec. However, the $E_{bias} = 0.8$ MeV bias of the stilbene detector, as applied via the detector

response function, should limit data points to $t < 711$ nsec²³. Currently, the effect of these three issues at late times is unknown, but it will be investigated in the near future.

3. Cryogenic Molecular Liquids: N_2

The simulated results and experimental data for a 1.1 mfp cryogenic liquid nitrogen (N_2) sphere are shown in **Figure 16**. The experimental data points are bracketed by the simulated results for the different nuclear data sets over the energy range $3 < E_n < 6$ MeV.

4. Molecular Solids: Teflon CF_2

The simulated results and experimental data for a 1.8 mfp Teflon (CF_2) sphere are shown in **Figure 17**. The agreement is quite good, except for energies $E_n < 1.5$ MeV, where the simulated results fall below the experimental data.

5. Isotopically Enriched Materials: 6Li , ${}^{235}U$ and ${}^{239}Pu$

The simulated results and experimental data for a 1.1 mfp 6Li sphere are shown in **Figure 18**. This is an excellent example of how differences in nuclear data sets can produce rather different time-of-flight spectra. The ENDL-94 and ENDL-2008.2 data sets provide excellent agreement with experimental data in the $2 < E_n < 12$ MeV energy range. The results obtained using the other nuclear data sets produce significantly lower spectra over that energy range. The high level of agreement between the data and the ENDL results is not surprising in light of the fact that the LLNL nuclear data team has historically utilized the pulsed sphere experimental data to constrain the ENDL data evaluations. This was, after all, one of the original motivations for the pulsed sphere program. For neutron energies in the range $1 < E_n < 2$ MeV, the JENDL-3.3 nuclear data set provides excellent agreement with the experimental data. Once again, the simulation results fall below the experimental data for $E_n < 1.5$ MeV.

The total and three largest partial cross sections for 6Li from the five evaluated nuclear data sets are shown in **Figure 19**. The curves are color coded by nuclear data set in the same manner as the time-of-flight spectral plots. For 6Li , the solid lines are the total, dashed lines are elastic scattering

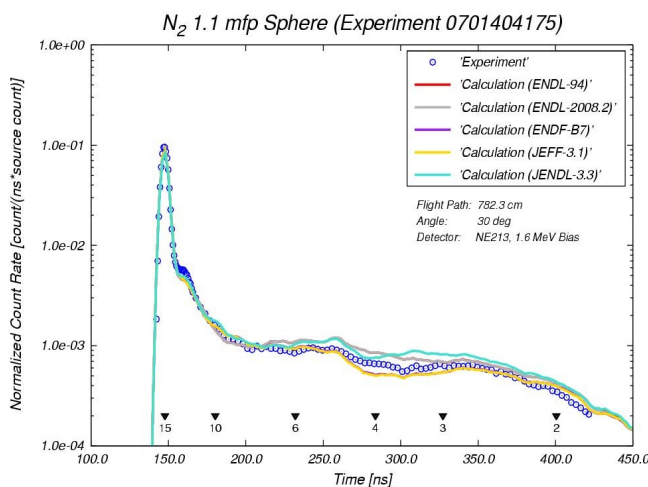


Fig. 16 The experimental and simulated time-of-flight spectra for a 1.1 mfp cryogenic liquid nitrogen (N_2) sphere.

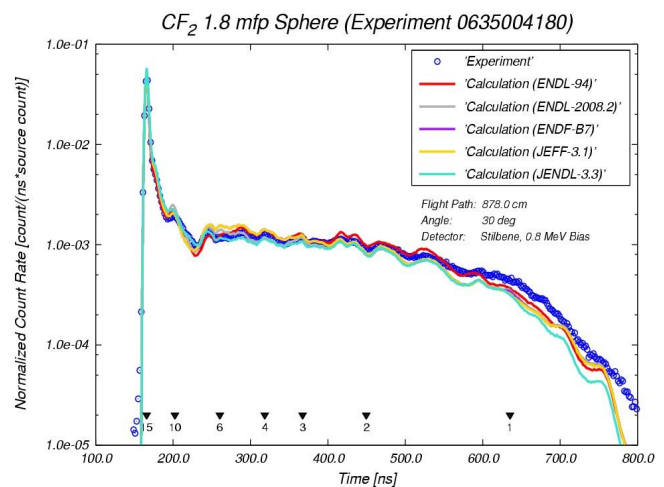


Fig. 17 The experimental and simulated time-of-flight spectra for a 1.8 mfp Teflon (CF_2) sphere.

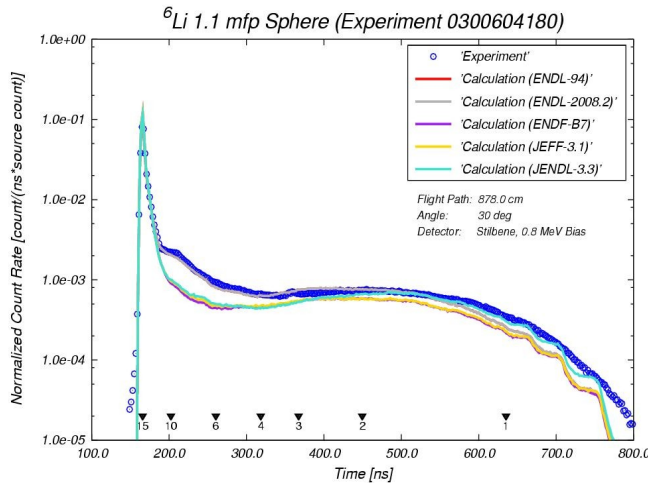


Fig. 18 The experimental and simulated time-of-flight spectra for a 1.1 mfp ${}^6\text{Li}$ sphere.

and dotted lines are (n,nd) reactions. Figure 19 shows ~15% difference in the evaluated elastic-scattering cross sections in the $2 < E_n < 12$ MeV energy range, where the ENDL data sets have the largest values. Similarly, over the energy range $1 < E_n < 2$ MeV, JENDL-3.3 has the largest elastic scattering cross section. These trends are consistent with the observed spectral behavior in those energy ranges. To further stress the differences in the evaluated nuclear data sets for ${}^6\text{Li}$, note that there is greater than a factor of three difference in the (n, nd) cross sections for energies $E_n > 2$ MeV.

The simulated results and experimental data for a 1.5 mfp ${}^{235}\text{U}$ sphere are shown in **Figure 20**. Significant differences are observed in the energy range $8 < E_n < 13$ MeV, where the simulated results are below the experimental data. As discussed in Reference 11, these differences have been attributed to inaccurate description of neutron emission in the preequilibrium and direct inelastic scattering in the ENDF/B-VI.6 nuclear data set, and presumably others as

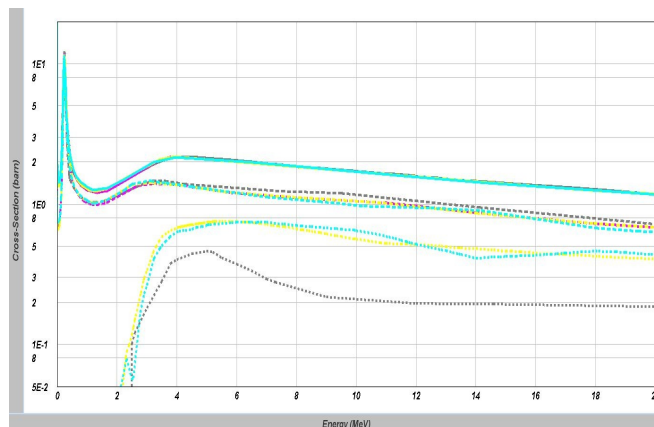


Fig. 19 Various neutron cross sections for ${}^6\text{Li}$ from the five evaluated nuclear data sets. The curves are color coded by nuclear data set in the same manner as the time-of-flight spectral plots. Solid lines are the total, dashed lines are elastic scattering and dotted lines are (n, nd) reactions.

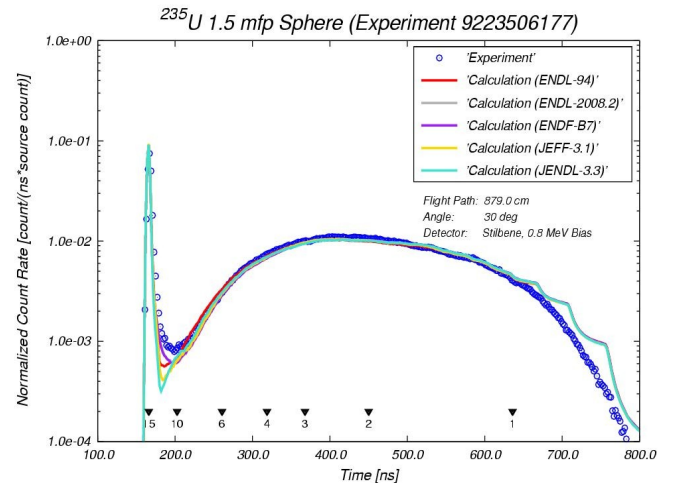


Fig. 20 The experimental and simulated time-of-flight spectra for a 1.5 mfp ${}^{235}\text{U}$ sphere.

well. These deficiencies have since been corrected in the development of the ENDF/B-VII data set, resulting in better agreement with the data when calculated with *MCNP*^{11,24}. This is evident in Figure 20, where the ENDF/B-VIII results are the closest to the experimental data, followed by both ENDL data sets. As before, the simulated results are well above the experimental data for energies $E_n < 1$ MeV.

The simulated results and experimental data for a 1.2 mfp ${}^{239}\text{Pu}$ sphere are shown in **Figure 21**. Overall, the plot resembles that in Figure 20. However, here the discrepancy between a subset of the results and the data in the energy range $8 < E_n < 13$ MeV is more pronounced. For this pulsed sphere, the order of agreement has flipped. The ENDL data sets provide the best level of agreement with the data over this energy range, those results being only slightly lower than the experimental data. Next comes the ENDF/B-VIII data set, which yields results that are up to ~30% lower than the data. It is interesting to note that for the ${}^{239}\text{Pu}$ sphere, the ENDL-94 results nearly overlays the data,

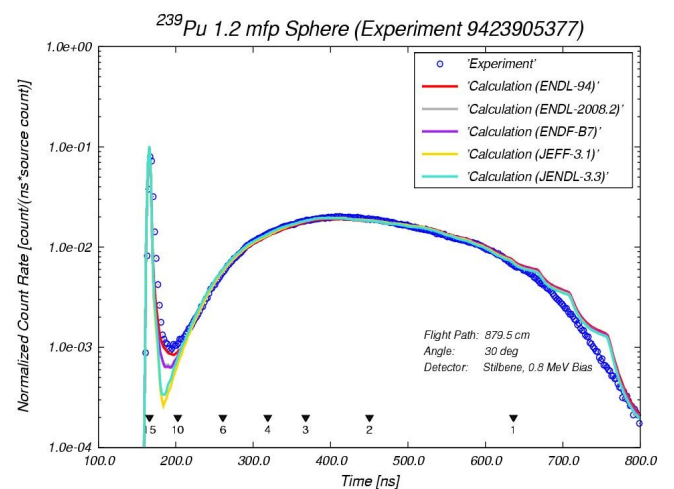


Fig. 21 The experimental and simulated time-of-flight spectra for a 1.2 mfp ${}^{239}\text{Pu}$ sphere.

indicating that the cross sections were tuned to match the data, while the same nuclear data applied to the ^{235}U sphere yields results that are $\sim 20\%$ lower than the data. Finally, the simulated results are above the experimental data for energies $E_n < 1$ MeV, but to a lesser degree than observed for the ^{235}U sphere.

6. Elemental Materials: Be and Fe

The simulated results and experimental data for a 0.8 mfp ^9Be (elemental beryllium is 100% ^9Be) sphere is shown in **Figure 22**. With the exception of the results obtained with the JEFF-3.1 data set, all of the results are in excellent agreement with the experimental data for $E_n > 1$ MeV. The differences between the results and data at low energies are similar to those already discussed. The anomalous JEFF-3.1 results below $E_n \sim 13$ MeV were a mystery until it was discussed with members of the nuclear data team at LLNL.

The Evaluated Nuclear Data Library (ENDL) used at LLNL is not only an evaluated nuclear data set, it is also a format for storing data within files. This situation is analogous to the Evaluated Nuclear Data File (ENDF). Most of the world's nuclear data set have adopted the ENDF data format, however, ENDL at LLNL has not. In order to provide access to other data sets at LLNL, the nuclear data team has developed a nuclear data translator known as *From ENDF To ENDL*, or **FETE**²⁵. This tool was developed to translate data between the two data formats in accordance with the documented ENDF format.

Unfortunately, the data evaluation team that provides the JEFF-3.1 data set used a non-standard technique for storing the double-differential $(f(E)f(\Omega))$ neutron emission data for the (n,2n) reaction¹². As a result, FETE was not able to translate the data and assumed that there was a zero probability for the (n,2n) reaction²⁶. This can be considered a problem with the processing of the evaluated data into a form that is suitable for use by a Monte Carlo code. Unfortunately, for users of the JEFF-3.1 data set at LLNL, there are no plans to modify **FETE** for support of such non-standard data files. Since this reaction is responsible for $\sim 1/3$ of the total cross section, over a wide range of incident

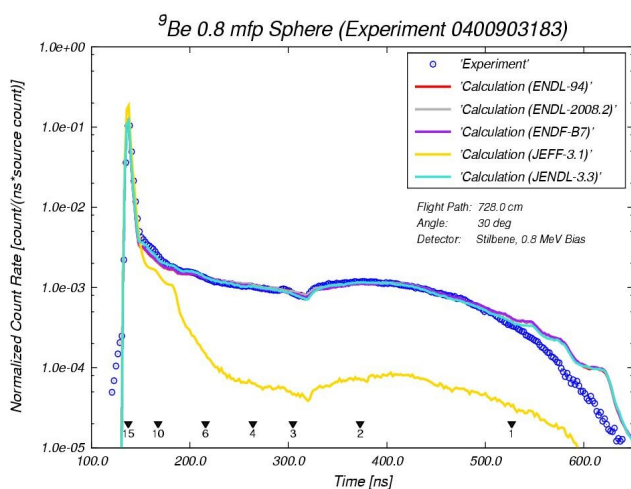


Fig. 22 The experimental and simulated time-of-flight spectra for a 0.8 mfp ^9Be sphere.

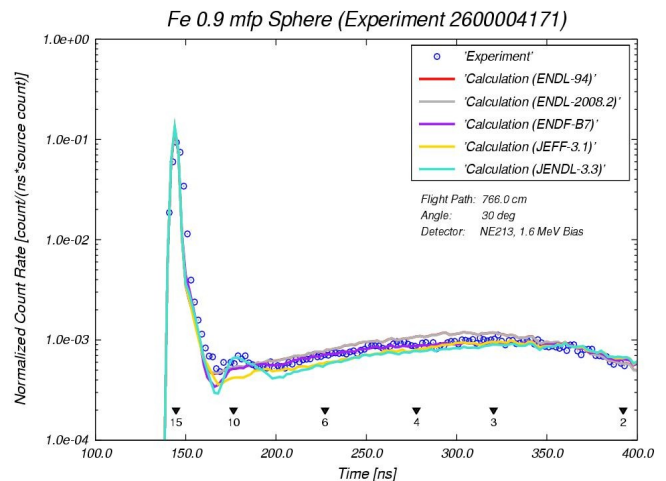


Fig. 23 The experimental and simulated time-of-flight spectra for a 0.9 mfp Fe sphere.

neutron energies, omission of the 2 outgoing neutrons for every third collision had a profound impact on the neutron economy of the problem. As a result, the JEFF-3.1 data set produces a time-of-flight spectrum that is too low by more than an order of magnitude at $E_n = 3$ MeV.

Finally, the simulated results and experimental data for a 0.9 mfp Fe sphere is shown in Figure 23. The level of agreement is quite good over the entire range of incident neutron energies. In addition, the simulation results bracket the experimental data over the energy range $3 < E_n < 8$ MeV.

V. Summary and Future Efforts

The **Mercury** Monte Carlo code has been used to perform modern calculations of fifty-six of the LLNL pulsed sphere experiments covering a broad range of sphere materials, optical depths and detector systems. Our model (utilizing biased-collision point-detector variance reduction methods and diagnostic particles) provides a more accurate representation of the experimental configuration than past efforts (which used a spherical representation of the experimental pit with a conical ring detector). These calculations were undertaken to (a) validate new features in the **Mercury** code, (b) demonstrate the ability of **Mercury** to model various time-of-flight diagnostic systems and (c) assess the quality of existing nuclear data evaluations. The simulated time-of-flight neutron spectra are generally in good agreement with experimental data. In particular, the timing and magnitude of the uncollided neutron peaks show excellent agreement, while the magnitude of the broad down-scattered and secondary-emission portion of the spectrum exhibit overall good agreement.

With regard to the quality of existing nuclear data evaluations, it appears that the ENDL-94 cross sections have been tuned to match the experimental data for several pulsed spheres. This study has also illustrated the following issues and discrepancies that are related to nuclear data. Modest computational differences have been observed relative to

experimental data for the ${}^6\text{Li}$, ${}^{235}\text{U}$ and ${}^{239}\text{Pu}$ spheres. In the case of ${}^6\text{Li}$, this can be attributed to an $\sim 15 - 20\%$ variation of the elastic scattering cross sections among data evaluations. With regard to the ${}^{235}\text{U}$ and ${}^{239}\text{Pu}$ spheres, differences in the time-of-flight spectra in the energy range $8 < E_n < 13$ MeV have been attributed to inaccurate representation of neutron emission from inelastic scattering processes in some of the data sets. To some degree, these discrepancies have been resolved with the release of the ENDF/B-VII data set. A significant issue in the translation of the ${}^9\text{Be}$ JEFF-3.1 data set between the ENDF and ENDL data formats has resulted in there being no (n,2n) cross sections available in the JEFF-3.1 data file at LLNL.

Several areas of additional effort are planned for the future. In an attempt to reconcile the differences in the simulated and experimental time-of-flight spectra at low energies, the *Mercury* pulsed sphere model will be modified to use the correct orientation of the deuteron beam, walls and collimator assembly for each specific experiment, as well as to limit comparisons to time ranges that are consistent with the detector bias applied in each experiment. As part of our efforts to validate the photon transport capabilities in *Mercury*, our team plans to compare simulated secondary-emission gamma spectra to direct measurements that used either liquid scintillator detectors and to spectra inferred from electron recoil spectroscopy^{2,4,6,3}. Finally, modeling of additional pulsed sphere experiments will be undertaken. Our goal is to simulate each experiment in the compendium of shots provided in Table 2 of Reference 18

Acknowledgment

The authors would like to acknowledge Alfredo Marchetti (for useful discussions and providing us with the file containing the pulsed sphere experimental data) and David Brown (for describing the details of the *FETE* data translation process and the non-standard use of the ENDF format for the JEFF-3.1 ${}^9\text{Be}$ (n,2n) neutron emission data). This work performed under the auspices of the U.S. Department of Energy by Lawrence Livermore National Laboratory under Contract DE-AC52-07NA27344.

References

- 1) C. Wong, J. D. Anderson, P. Brown, L. F. Hansen, J. L. Kammerdiener, C. Logan and B. Pohl, *Livermore Pulsed Sphere Program: Program Summary Through July 1971*, UCRL-51144, Revision 2, Lawrence Livermore National Laboratory (1972).
- 2) G. S. Sidhu, W. E. Farley, L. F. Hansen, T. T. Komoto, B. A. Pohl and C. Wong, "Neutron and Gamma Radiation from a Nitrogen Sphere Surrounding a D-T Neutron Source". *Nucl. Sci. Eng.*, **63**, 48 - 54 (1977).
- 3) L. F. Hansen, T. Komoto, E. F. Plechaty, B. A. Pohl, G. S. Sidhu and C. Wong, "Measurements and Calculations of the Electron Recoil Spectra From Gamma Rays Emitted by Nitrogen for a 14MeV Source". *Nucl. Sci. Eng.*, **62**, 550 - 558 (1977).
- 4) L. F. Hansen, C. Wong, T. T. Komoto, B. A. Pohl, E. Goldberg, R. J. Howerton and W. M. Webster, "Neutron and Gamma Spectra from ²³²Th, ²³⁵U, ²³⁸U and ²³⁹Pu After Bombardment with 14MeV Neutrons". *Nucl. Sci. Eng.*, **72**, 35 - 49 (1979).
- 5) L. F. Hansen, H. M. Blann, R. J. Howerton, T. T. Komoto and B. A. Pohl, "The Transport of 14 MeV Neutrons Through Heavy Materials 150 < A < 208". *Nucl. Sci. Eng.*, **92**, 382 - 396 (1986).
- 6) E. Goldberg, L. F. Hansen, T. T. Komoto, B. A. Pohl, R. J. Howerton, R. E. Dye, E. F. Plechaty and W. E. Warren, "Neutron and Gamma Ray Spectra from a Variety of Material Bombarded with 14 MeV Neutrons". *Nucl. Sci. Eng.*, **105**, 319 - 335 (1990).
- 7) Mercury Code Team, "Mercury Web Site", Lawrence Livermore National Laboratory, <http://www.llnl.gov/mercury>
- 8) R.J. Procassini, P. S. Brantley, S. A. Dawson, G. M. Greenman, M. S. McKinley and M. J. O'Brien, *Mercury User Guide: Version c.8*, UCRL-TM-204296, Revision 7, Lawrence Livermore National Laboratory (2010).
- 9) D. A. Resler, R. J. Howerton and R. M. White, "Benchmark Comparisons of Evaluated Nuclear Data Files", *Proceedings, International Conference on Nuclear Data for Science and Technology*, 9 - 13 May 1994, Gatlinburg, TN (1994).
- 10) D. A. Brown, M. A. Descalle, R. Hoffman, K. Kelley, P. Navratil, J. A. Pruet, N. C. Summers, I. J. Thompson and R. Vogt, *Release of the 2008 Evaluated Nuclear Data Library (ENDL2008)*, LLNL-TR-413190, Lawrence Livermore National Laboratory (2009).
- 11) M.B. Chadwick, P. Obložinský, M. Herman, N.M. Greene, R.D. McKnight, D.L. Smith, P.G. Young, R.E. MacFarlane, G.M. Hale, S.C. Frankle, A.C. Kahler, T. Kawano, R.C. Little, D.G. Madland, P. Moller, R.D. Mosteller, P.R. Page, P. Talou, H. Trellue, M.C. White, W.B. Wilson, R. Arcilla, C.L. Dunford, S.F. Mughabghab, B. Pritychenko, D. Rochman, A.A. Sonzogni, C.R. Lubitz, T.H. Trumbull, J.P. Weinman, D.A. Brown, D.E. Cullen, D.P. Heinrichs, D.P. McNabb, H. Derrien, M.E. Dunn, N.M. Larson, L.C. Leal, A.D. Carlson, R.C. Block, J.B. Briggs, E.T. Cheng, H.C. Huria, M.L. Zerkle, K.S. Kozier, A. Courcelle, V. Pronyaev and S.C. van der Marck, "ENDF/B-VII.0: Next Generation Evaluated Nuclear Data Library for Nuclear Science and Technology". *Nucl. Data Sheets*, **107**, 2931 - 3060 (2006).
- 12) A. Koning, R. Forrest, M. Kellett, R. Mills, H. Henriksson and Y. Rugama, *The JEFF-3.1 Nuclear Data Library*, NEA/6190, Nuclear Energy Agency (2006).
- 13) K. Shibata, T. Kawano, T. Nakagawa, O. Iwamoto, J. Katakura, T. Fukahori, S. Chiba, A. Hasegawa, T. Murata, H. Matsunobu, T. Ohsawa, Y. Nakajima, T. Yoshida, A. Zukeran, M. Kawai, M. Baba, M. Ishikawa, T. Asami, T. Watanabe, Y. Watanabe, M. Igashira, N. Yamamuro, H. Kitazawa, N. Yamano and H. Takano, "Japanese Evaluated Nuclear Data Library Version 3 Revision-3: JENDL-3.3". *J. Nucl. Sci. Technol.*, **39**, 1125 - 1136 (2002).
- 14) A. A. Marchetti and G. W. Hedstrom, *New Monte Carlo Simulations of the LLNL Pulsed-Sphere Experiments*, UCRL-ID-131461, Lawrence Livermore National Laboratory (1998).
- 15) D. J. Whalen, D. A. Cardon, J. L. Uhle and J. S. Hendricks, *MCNP: Neutron Benchmark Problems*, LA-12212, Los Alamos National Laboratory (1991).
- 16) P. G. Young, M. B. Chadwick, R. E. MacFarlane, P. Talou, T. Kawano, D. G. Madland, W. B. Wilson and C. W. Wilkerson, "Evaluation of Neutron Reactions for ENDF/B-VII: 232-241U and 239Pu". *Nucl. Data Sheets*, **108**, 2589 - 2654 (2007).
- 17) C. J. Keane, "Overview - NIF Diagnostics and the National Ignition Campaign", Lawrence Livermore National Laboratory, https://lasers.llnl.gov/for_users/experimental_capabilities/diagnostics.php
- 18) J. A. Bucholz and S. C. Frankle, "Improving the LLNL Pulsed Sphere Experiments Database and MCNP Models", *Proceedings, American Nuclear Society Summer Meeting*, 1 - 5 June 2003, San Diego, CA (2003).
- 19) J. F. Ziegler, "TRIM Version 96: The Stopping and Range of Ions in Matter", <http://www.research.ibm.com/ionbeams>
- 20) S. J. Bame and B. E. Perry, "FIND THE TITLE". *Phys. Rev.*, **107**, 1616 - 1629 (1957).
- 21) D.E. Cullen, *TART 2005: A Coupled Neutron-Photon 3-D, Combinatorial Geometry Time Dependent Monte Carlo Transport Code*, UCRL-SM-218009, Lawrence Livermore National Laboratory (2005).
- 22) S. C. Frankle, *LLNL Pulsed Sphere Measurements and Detector Response Functions*, X-5:SCF-04-004, Los Alamos National Laboratory (2004).
- 23) S. C. Frankle, *LLNL Pulsed Sphere Measurements and Detector Response Functions*, LA-UR-05-5878, Los Alamos National Laboratory (2004).
- 24) X-5 Monte Carlo Code Team, *MCNP — A General Monte Carlo N-Particle Transport Code, Version 5, Volume II: User's Guide*, LA-CP-03-0245, Los Alamos National Laboratory (2003).
- 25) D. A. Brown, G. W. Hedstrom and A. Hill, *User's Guide to FETE: From ENDF To ENDL*, UCRL-SM-218496, Lawrence Livermore National Laboratory (2006).
- 26) D. A. Brown, Lawrence Livermore National Laboratory, private communication (2010).